Computers and Fluids 139 (2016) 92–104

Contents lists available at ScienceDirect

Computers and Fluids

journal homepage: www.elsevier.com/locate/compfluid

A priori and a posteriori evaluations of sub-grid scale models for the Burgers' equation

Yanan Li [a,*], Z.J. Wang [b]

[a] Department of Aerospace Engineering, AIAA Member, University of Kansas, Lawrence, KS, 66045
[b] Department of Aerospace Engineering, AIAA Fellow, University of Kansas, Lawrence, KS, 66045

ARTICLE INFO

Article history:
Received 15 October 2015
Revised 11 April 2016
Accepted 13 April 2016
Available online 14 April 2016

Keywords:
Large eddy simulation
High-order schemes
Flux reconstruction method
Sub–grid scale models

ABSTRACT

In large eddy simulations (LES) of turbulent flows, large scale motions are resolved by the numerical simulation while the effect of the small scale motions is represented as sub-grid scale (SGS) stresses computed with SGS models. In the present study, we perform a priori and a posteriori evaluations of five SGS models for the one dimensional Burgers' equation with the high-order flux reconstruction (FR) or correction procedure via reconstruction (CPR) approach. It is shown that all models, except the scale similarity model (SSM) and the mixed model (MM), demonstrate very little correlation with the DNS results. The stability of the SSM is investigated. The effects of numerical dissipation and the models' influence on LES are discussed. Based on the present study, we advocate the use of implicit LES (ILES) in LES in the context of discontinuous high-order methods, or any numerical methods with built-in numerical dissipation.

1. Introduction

Large eddy simulations (LES) have been used in the computation of turbulent flows for decades because of the potential in resolving multiple turbulence scales. As a comparison, Reynolds-averaged Navier-Stokes (RANS) approaches model all scales of turbulence, while direct numerical simulation (DNS) approaches resolve all turbulence scales. Although RANS models have been effective for many practical problems, they have difficulty handling complex massively separated unsteady flows. The use of DNS in computing high Reynolds number flows is also, for the foreseeable future, limited by computing power [1]. LES is a compromise of the two approaches, and offers the best promise for vortex dominated separated flows. In LES, large scales and small scales are separated by a low-pass filter. The large scales are resolved while the effect of small scales is represented by an explicit sub-grid scale (SGS) stress model. Since small-scale motions are believed to be more universal, and thus easier to model than large scales ones, LES offers reasonable accuracy even for unsteady separated flows while requiring much less computer resources than DNS [2].

Many SGS models have been developed in the last four decades. This paper focuses on five of them: the static Smagorinsky model (SS) [3,4], the dynamic Smagorinsky model (DS) [5], the scale-similarity model (SSM) [10], the mixed model (MM) [10], and the linear unified RANS-LES model (LUM) [34]. Among explicit models, the SS is a popular one because of its simplicity. The effect of the SGS stress upon the resolved scales is modeled as an eddy viscosity. The eddy viscosity is expressed in the mixing length form with a dimensionless empirical coefficient. However, it has been found that the empirical coefficient depends on the flow. It also adds too much dissipation to the large scale motions if we keep the coefficient the same as we approach wall boundaries. To resolve these deficiencies, the DS model was developed [5]. In the DS model, the coefficient is calculated based on the Germano identity, which involves two levels of filtering and relates the SGS stress to the resolved stress. The coefficient is locally decided and no longer a prescribed constant, and it goes to zero as a wall boundary is approached. The DS model has been applied to a large variety of flow simulations [6–9].

An alternative way to model the SGS stress is offered by the SSM [10]. As the name indicates, it assumes similarity between two scales of stresses, the resolved stress and the SGS stress. Numerical tests showed that energy accumulated at small scales with this model [11]. To remedy the problem, the DS was added to dissipate the energy, which led to the MM.

Recently, hybrid RANS-LES models have received much research interest. They combine RANS with LES so that in the near wall region, the RANS model is used, while LES is employed in the outer region. These models have demonstrated good accuracy with reasonable cost when compared to a pure LES approach. The linear unified RANS-LES model (LUM) was developed in [34]. In the present work, we also evaluate the LUM model.

* Corresponding author. Tel.: +15157084718.
E-mail addresses: yananli@ku.edu (Y. Li), zjw@ku.edu (Z.J. Wang).

http://dx.doi.org/10.1016/j.compfluid.2016.04.015
0045-7930/

Nomenclature

u	the state variable
ν	viscosity
τ^{SGS}	sub-grid scale stress
Δ	first filter width
G_Δ	filter kernel
Δx_{DNS}	DNS cell size
Δx_{LES}	LES cell size
ν^{SGS}	sub-grid scale viscosity
S_{ij}	rate of strain
c_s	the Smagorinsky model coefficient
c_{ssm}	the scale-similarity model coefficient
L_{ij}	resolved stress
$\tilde{\Delta}$	test filter width
γ	ratio of the test filter width over the LES filter width
k_t	turbulent kinetic energy
ω	specific dissipation
τ_L	time scale of linear unified model
ν_t	modeled viscosity of linear unified model
l_*	constant of linear unified model
k	wave number
α	lifting constants of correction procedure via reconstruction method
$r_f^{\pm}$	corrections to the gradients
Δt	time step
E	turbulent kinetic energy
w	weight coefficient of filtering
L_i	shape function
β	phase angle
S_R	smallest resolved scale

Finally, we also consider the monotone integrated LES [2] or implicit LES (ILES) [14], in which no explicit SGS model is used. In ILES, the numerical algorithm has its numerical dissipation which serves as the SGS. The obvious advantage of ILES is its lower computational cost compared with the conventional SGS models.

Because of the disparate length scales in a turbulent flow, high order methods are often preferred to compute the large scales because of their high accuracy. The flux reconstruction (FR) or correction procedure via reconstruction (CPR) was recently developed in [12], and extended to hybrid meshes and two and three dimensions in [13,26–33]. The FR/CPR formulation is among the most efficient discontinuous methods for it gives high accurate simulation results with a relatively low cost of computing power and storage.

The large eddy simulation of decaying homogeneous isotropic turbulence with the FR/CPR method was conducted recently [38]. The ILES approach always produces better results than the static or dynamic Smagorinsky model through comparison with the DNS results. Fig. 1 shows the comparison of the normalized dissipation rate. Fig. 2 shows the energy spectra at two different times. From both figures, we see that on a given coarse mesh, ILES yields more accurate results than the LES with the Smagorinsky models.

To understand the reason, all the SGS models are evaluated with the one dimensional Burgers' equation rather than the full Navier Stokes equations. The 1D Burgers' equation is not a model for the 3D turbulence, but it is still a good one for assessing the SGS models because of its nonlinear convection term. We initialize the simulations mimicking a typical turbulence energy spectrum in the Fourier space with random phase angles. The FR/CPR method is used to discretize the Burgers' equation and the explicit three-stage SSP Runge Kutta scheme [37] is employed for time integration.

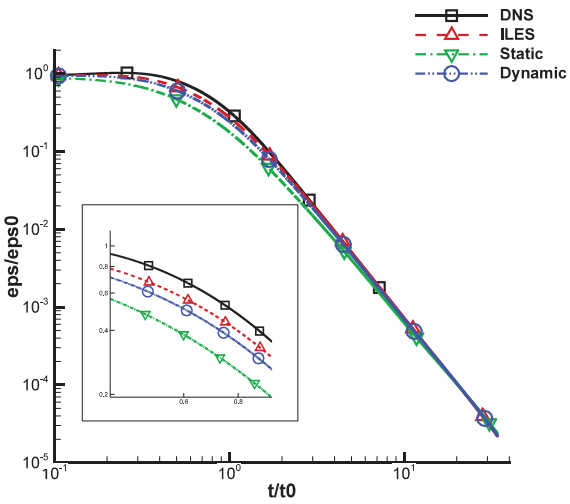

Fig. 1. Normalized dissipation rate.

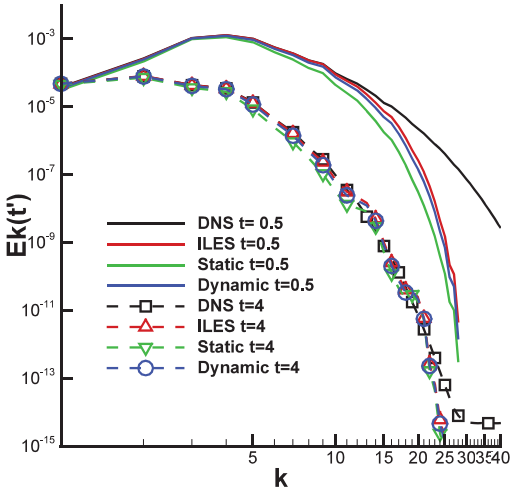

Fig. 2. The energy spectra at non-dimensional time 0.25 and 4.

This paper is organized as follows. In the next Section, the governing equation for the one-dimensional Burgers' equation is given and the SGS stress models are briefly reviewed and derived for the one dimensional Burgers' equation. In Section 3, the numerical method is briefly reviewed. In Section 4, the numerical results are presented and discussed. Finally, the conclusions from the present study are given in Section 5.

2. Governing equation and SGS models

To evaluate the SGS models, in this paper, we consider the one dimensional Burgers' equation,

$$\frac{\partial u}{\partial t} + u\frac{\partial u}{\partial x} = \nu\frac{\partial^2 u}{\partial x^2}, \qquad x \in [-1, 1] \tag{1}$$

where u is the state variable such as velocity, ν is a constant viscosity. In the present study, $\nu = 8E-05$ is chosen to imitate a high Reynolds number flow problem. Next, we apply a low-pass spatial filter, $G_\Delta(x, \xi)$ to the equation satisfying the following conservative property

$$\int_{-\infty}^{+\infty} G_\Delta(x,\xi)d\xi = 1, \tag{2}$$

where Δ denotes the filter width. A typical filter, the box filter, is defined below,

$$G_\Delta(x,\xi) = \begin{cases} 1/\Delta & |x-\xi| \le \Delta/2 \\ 0 & otherwise \end{cases}. \tag{3}$$

The filtering process is defined mathematically in the physical space as a convolution operator. The filtered variable $\hat{\phi}(x,\ t)$ of a space-time variable $\phi(x,\ t)$ in 1D is defined as

$$\hat{\phi}(x,\ t) = \int_{-\infty}^{+\infty} G_\Delta(x,\xi)\phi(\xi,t)d\xi. \tag{4}$$

The filtering process is linear, i.e. $\widehat{\phi+\varphi} = \hat{\phi}+\hat{\varphi}$. If the filter width is constant, the differential and the filter operators commute, i.e., $\frac{\partial\hat{\phi}}{\partial x} = \frac{\partial\hat{\phi}}{\partial x}$. In the present study, all the filtering processes are done with the box filter on a uniform mesh. After applying the filter to Eq (1), we obtain

$$\frac{\partial\hat{u}}{\partial t} + \hat{u}\frac{\partial\hat{u}}{\partial x} = \nu\frac{\partial^2\hat{u}}{\partial x^2} - \frac{\partial\left(\frac{1}{2}\widehat{uu} - \frac{1}{2}\hat{u}\hat{u}\right)}{\partial x}. \tag{5}$$

The unclosed term arises due to the filtering of the nonlinear convection term

$$\boldsymbol{\tau}^{SGS} = \frac{1}{2}\widehat{uu} - \frac{1}{2}\hat{u}\hat{u}. \tag{6}$$

This is the SGS of the Burgers' equation.

SGS models act as the closure of the governing equation. In this section we review several SGS models and translate them to work for the Burgers' equation.

2.1. Static Smagorinsky model

The SS is in the eddy viscosity form. For 3D incompressible flow, the SGS stress is defined as,

$$\tau_{ij}^{SGS} = -2\nu_{SGS}\hat{S}_{ij}, \tag{7}$$

where $\hat{S}_{ij}$ is the resolved rate-of-strain tensor

$$\hat{S}_{ij} = \frac{1}{2}\left(\partial_i\hat{u}_j + \partial_j\hat{u}_i\right). \tag{8}$$

The SGS viscosity, ν_{SGS}, is modeled following the mixing length idea

$$\nu_{SGS} = (c_s\Delta)^2\sqrt{2\left|\hat{S}\right|^2}, \tag{9}$$

where $|\hat{S}|^2 = \hat{S}_{ij}\hat{S}_{ji}$, c_s is the prescribed coefficient. By comparing the mean SGS dissipation from DNS data and the modeled SGS dissipation, c_s can be determined. Lilly used this procedure for isotropic turbulence to obtain $c_s = 0.16$ [4].

The SS was described by Moin and Kim [15], Rogallo and Moin [16], Lesieur and Metais [17] and Pope [18]. The deficiency of this model first showed up in the comparison of the modeled SGS stress and the true SGS stress computed from the DNS solution by Clark et al. [19], McMillan and Ferziger [20], and Bardina et al. [10]. The comparisons imply that the model does not capture the SGS adequately. In [11], Meneveau et al. gave an explanation of this problem. Another weakness of this model is that it gives non-zero eddy viscosity in laminar-flow regions. Therefore a wall function is needed to damp the SGS viscosity in a wall-bounded flow.

Next, we derive its 1D formulation. The rate of strain in 1D is

$$\hat{S} = \partial_x\hat{u}. \tag{10}$$

The SGS viscosity is then

$$\nu_{SGS} = (c_s\Delta)^2\left|\partial_x\hat{u}\right|. \tag{11}$$

Therefore the SGS stress becomes

$$\tau^{SGS} = -\nu_{SGS}\hat{S}. \tag{12}$$

2.2. Dynamic Smagorinsky model

The model coefficient, c_s, in SS is prescribed. However, it is found empirically that c_s depends on the flow, being 0.1 for the plane channel flow and 0.2 for isotropic turbulence [2]. The DS makes it a variable spatially and temporally. It introduces a test filter to the resolved scales and uses the assumption of scale invariance to compute the model coefficient. As the model for three dimensional turbulence is readily available, we derive it for the 1D Burgers' equation next.

Following Eq. (5), we consider the 2nd filter with width $\tilde{\Delta}$, defined as $\tilde{\Delta} = \gamma\Delta$, $\gamma \ge 1$. By applying this filter to the SGS stress, we obtain

$$\tilde{\boldsymbol{\tau}}^{SGS} = \frac{1}{2}\widetilde{\widehat{uu}} - \frac{1}{2}\widetilde{\hat{u}\hat{u}}. \tag{13}$$

By applying the second filter to the LES solution, we obtain the resolved stress,

$$L = \frac{1}{2}\widetilde{\hat{u}\hat{u}} - \frac{1}{2}\widetilde{\hat{u}}\widetilde{\hat{u}}. \tag{14}$$

The Germano identity can be written as

$$T = \tilde{\boldsymbol{\tau}}^{SGS} + L, \tag{15}$$

where $T = \widetilde{\widehat{uu}} - \widetilde{\hat{u}}\widetilde{\hat{u}}$. We apply the SS to both T and τ and assume they share the same coefficient, c_s

$$-\left(c_s\tilde{\Delta}\right)^2\left|\partial_x\widetilde{\hat{u}}\right|\partial_x\widetilde{\hat{u}} = -(c_s\Delta)^2\widetilde{\left|\partial_x\hat{u}\right|\partial_x\hat{u}} + L. \tag{16}$$

We define

$$M = \Delta^2\widetilde{\left|\partial_x\hat{u}\right|\partial_x\hat{u}} - \tilde{\Delta}^2\left|\partial_x\widetilde{\hat{u}}\right|\partial_x\widetilde{\hat{u}}. \tag{17}$$

Thus ${c_s}^2 = \frac{L}{M}$. It is assumed that c_s is spatially uniform so that it can be extracted from the test-filtering operation (Ghosal et al 1995) [21]. In the 1D test, we take the most common choice of $\gamma = 2$.

In three dimensions, this is an over-determined system. To minimize the square error, Lilly used the following approach

$${c_s}^2 = \frac{\langle L_{ij}M_{ij}\rangle}{\langle M_{ij}M_{ij}\rangle}, \tag{18}$$

where $\langle\ \cdot\ \rangle$ means averaging along the homogeneous direction. The DS gives a highly variable eddy viscosity field [22] including negative values which makes the simulation unstable. Averaging over homogeneous directions was used by Germano et al. [5] to prevent this problem. Ghosal et al. [21] showed that this procedure minimizes the total error in the homogeneous region over which the averaging is performed. With these modifications, the eddy viscosity still can be negative. So the value of ${c_s}^2$ is clipped to be non-negative. In 1D, we don't have these problems. Thus we don't use a least squares averaging operation. But we still require ${c_s}^2$ to be non-negative.

2.3. Scale-similarity model

The SSM was first introduced by Bardina et al. [10]. It assumes scale invariance between the computable stress L and the SGS stress τ^{SGS}. This assumption was verified with empirical band pass-filtered PIV measurements by Liu et al. [23]. It suggests that τ^{SGS} is similar to a stress constructed from the resolved scales,

$$\tau^{SGS} = c_{ssm}L, \tag{19}$$

where L is the resolved stress, which is given in Eq. (14).

Many different second filter widths were suggested by various researchers. The Bardina's original model uses the same filter width for the two filters, i.e., $\Delta = \tilde{\Delta}$, and $\gamma = 1$. Liu et al used

$\gamma = 2$ and Akhavan et al use $\gamma = \frac{4}{3}$ [24]. The coefficient c_{ssm} is empirical and found to be close to 1. In the 1D test, c_{ssm} is adjusted to be 0.25 with $\gamma = 2$, based on an analysis performed in [36].

In [10], the true and modeled stresses showed a high degree of correlation in Bardina et al's a priori tests, and the SSM allowed for energy backscatter. However, this model was found to be not sufficiently dissipative. Energy accumulated at small scales leading to possible numerical instability. In the present study, we will duplicate this result with a non-dissipative numerical scheme, and will show that the phenomenon does not occur with the dissipative FR/CPR method.

2.4. Mixed model

To resolve the above-mentioned problem of the SSM, the DS is included in the formulation to add extra dissipation. In three dimensions, the mixed model (MM) is

$$\tau_{ij}^{SGS} = c_{ssm} L_{ij} - 2\nu_{SGS}\hat{\bar{S}}_{ij}. \tag{20}$$

Liu et al. [23] showed that the magnitude of the similarity term is much larger than that of the dissipative DS term. Hence, the high correlation of the SSM is not degraded by the extra viscosity. Zang et al. [39] used this model for recirculating flows with $\gamma = 1$. Wu & Squires applied this model successfully with Lagrangian averaging in simulations of 3D boundary layers [25]. There are dynamic ways to determine c_{ssm} as well. Vreman et al. [40] proposed a two-parameter dynamic MM in which c_s and c_{ssm} are both calculated dynamically with $\gamma = 1$.

In the present one dimensional study, the values $c_{ssm} = 0.25$ and $\gamma = 2$ are used. The SGS stress is defined as

$$\tau = c_{ssm}\left(\frac{1}{2}\widetilde{\hat{u}\hat{u}} - \frac{1}{2}\widetilde{\hat{u}}\widetilde{\hat{u}}\right) - \nu_{SGS}\hat{\bar{S}}. \tag{21}$$

The numerical instability of the SSM model is not a problem for numerical schemes with embedded numerical dissipation. It is shown in Section 4.

2.5. Linear unified RANS-LES model

The wall-bounded turbulent flows at high Reynolds numbers are a significant challenge for LES. The near wall region requires a high resolution grid to resolve the small energetic scales. The linear unified RANS-LES model (LUM) combines RANS with LES to solve this problem. The model equations for incompressible flows are

$$\begin{cases} \dfrac{\tilde{D}\tilde{U}_i}{\tilde{D}t} = -\dfrac{\partial\left(\dfrac{p}{\rho} + \dfrac{2k_t}{3}\right)}{\partial x_i} + 2\dfrac{\partial(\nu+\nu_t)\tilde{S}_{ik}}{\partial x_k} \\ \dfrac{\tilde{D}k_t}{\tilde{D}t} = -\dfrac{\partial\left((\nu+\nu_t)\dfrac{\partial k_t}{\partial x_i}\right)}{\partial x_i} + \nu_t S^2 - 2\dfrac{(1-c_0)k_t}{\tau_L}, \\ \dfrac{\tilde{D}\omega}{\tilde{D}t} = C_{\omega 1}\dfrac{\omega}{k}\nu_t S^2 - \dfrac{C_{\omega 2}}{C_k}\omega^2 + \dfrac{\partial\left(\left(\nu + \dfrac{\nu_t}{\sigma_\omega}\right)\dfrac{\partial\omega}{\partial x_j}\right)}{\partial x_j} \\ \qquad + \dfrac{C_\omega}{k}(\nu+\nu_t)\dfrac{\partial k_t}{\partial x_j}\dfrac{\partial\omega}{\partial x_j} \end{cases} \tag{22}$$

where $\tilde{D}/\tilde{D}t = \partial/\partial t + \tilde{U}_k\partial/\partial x_k$. $C_{\omega 1}$, $C_{\omega 2}$, C_ω, C_k, c_0 and σ_ω are all model constants, $\tilde{U}_i$ is the filtered velocity, k_t is the turbulent kinetic energy, ω is the specific dissipation, τ_L is the time scale and ν_t is the modeled viscosity. In this work, we only focus on the LES aspect of the model. Therefore τ_L is calculated with $\tau_L = l_*\Delta/k^{\frac{1}{2}}$, where $l_* = 1/3$. In summary, for the one-dimensional Burgers' equation, we solve

$$\begin{cases} \dfrac{\hat{D}\hat{u}}{\hat{D}t} = \dfrac{\partial(\nu+\nu_t)\dfrac{\partial\hat{u}}{\partial x}}{\partial x} \\ \dfrac{\hat{D}k_t}{\hat{D}t} = -\dfrac{\partial\left((\nu+\nu_t)\dfrac{\partial k_t}{\partial x}\right)}{\partial x} + 2\nu_t\left(\dfrac{\partial\hat{u}}{\partial x}\right)^2 - 2\dfrac{(1-c_0)k_t}{\tau_L} \end{cases} \tag{23}$$

where $\nu_t = \frac{k_t\tau_L}{3}$, $\tau_L = l_*\Delta/k_t^{\frac{1}{2}}$.

3. Numerical method and simulation conditions

3.1. Space discretization

Huynh [12] developed a high-order FR/CPR formulation, which was later employed for the Navier-Stokes equations on hybrid 3D meshes [26]. It has been used for 1D, 2D and 3D laminar and turbulent flows. Validations and successful applications can be found in [27–33]. In this study, we apply the 3rd order FR/CPR scheme to the 1D Burgers' equation and evaluate its performance with various SGS models.

The FR/CPR formulation for the inviscid 1D Burgers' equation is given as

$$\frac{\partial u_{i,j}}{\partial t} + \Pi_j\left(\frac{\partial F(u_i)}{\partial x}\right) + \frac{1}{\Delta x_i}\left(\alpha_{R,j}[F^n]_{i+1/2} + \alpha_{L,j}[F^n]_{i-1/2}\right) = 0, \tag{24}$$

where u_{ij} is the solution at solution point j of element i, u_i is the solution polynomial for element i,, $\Pi_j(\frac{\partial F(u_i)}{\partial x})$ denotes the projected flux derivative at the solution point, Δx_i is the length of element i, $[F^n]_{i+1/2}$ and $[F^n]_{i-1/2}$ are the differences between the local flux and the common Riemann flux at the right and left interfaces of element i, $\alpha_{R,j}$ and $\alpha_{L,j}$ are the correction coefficients independent of the solution variables.

For the viscous term on the right hand side of Burgers' equation, we follow the BR2 approach [35]. The 1D version is described below. First we introduce a new variable $R = \frac{\partial u}{\partial x}$. The corrected gradient is then

$$R_{i,j} = \frac{\partial u_{i,j}}{\partial x} + \frac{1}{\Delta x_i}\left(\alpha_{R,j}[u^{com} - u_i]_{i+1/2} + \alpha_{L,j}[u^{com} - u_i]_{i-1/2}\right), \tag{25}$$

where $[\boldsymbol{u^{com}}]_{\boldsymbol{i}+1/2}$ and $[\boldsymbol{u^{com}}]_{\boldsymbol{i}-1/2}$ are the common solutions at interfaces, $[\boldsymbol{u_i}]_{\boldsymbol{i}+1/2}$ and $[\boldsymbol{u_i}]_{\boldsymbol{i}-1/2}$ are the solutions from element i at the interfaces. The common solution is defined as

$$u_{i+1/2}^{com} = \frac{u_{i+1/2}^{-} + u_{i+1/2}^{+}}{2}, \tag{26}$$

where $u_{i+1/2}^{-} = [u_i]_{i+1/2}$ and $u_{i+1/2}^{+} = [u_{i+1}]_{i+1/2}$ are the solutions at the left and right sides of interface i+1/2. Next, the viscous flux, $F^v = \nu\frac{\partial u}{\partial x}$, at solution points can be calculated by

$$F_{i,j}^{v} = F^v\left(R_{i,j}\right). \tag{27}$$

Then $\frac{\partial F^v}{\partial x}$ can be obtained by using the Lagrange polynomial approach. The common viscous flux at the interface is needed to correct $\frac{\partial F^v}{\partial x}$ at solution points,

$$F_{i+1/2}^{v,com} = \nu\left(\frac{\partial u}{\partial x}\right)_{i+1/2}^{com}. \tag{28}$$

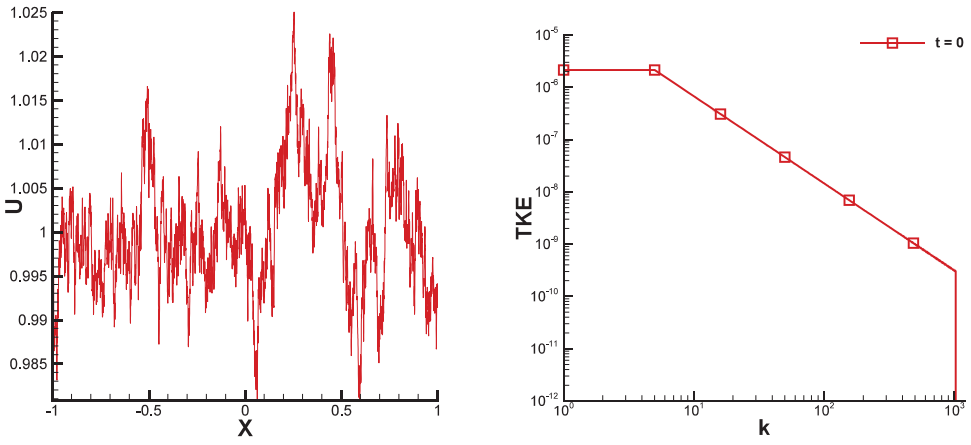

Fig. 3. Initial condition(left) and the initial energy spectrum(right).

For the common gradient,

$$\left(\frac{\partial u}{\partial x}\right)^{com}_{i+1/2} = \frac{1}{2}\left(\left(\frac{\partial u}{\partial x}\right)^{-}_{i+1/2} + r^{-}_{i+1/2} + \left(\frac{\partial u}{\partial x}\right)^{+}_{i+1/2} + r^{+}_{i+1/2}\right). \tag{29}$$

where $(\frac{\partial u}{\partial x})^{-}_{i+1/2}$ and $(\frac{\partial u}{\partial x})^{+}_{i+1/2}$ are the gradients of the solution of the left and right cells with no correction, $r^{-}_{i+1/2}$ and $r^{+}_{i+1/2}$ are the corrections to the gradients due to the common solution at the interface. More specifically, the corrections are,

$$r^{-}_{i+1/2} = \frac{1}{\Delta x_i}\left(\alpha^{-}\left[u^{com} - u^{-}\right]_{i+1/2}\right), \tag{30}$$

$$r^{+}_{i+1/2} = \frac{1}{\Delta x_{i+1}}\left(\alpha^{+}\left[u^{com} - u^{+}\right]_{i+1/2}\right), \tag{31}$$

where $\boldsymbol{\alpha}^{-}$ and $\boldsymbol{\alpha}^{+}$ are the interface correction coefficients.

3.2. Temporal discretization

The explicit SSP three-stage 3rd order Runge-Kutta scheme [37] is used as the temporal discretization. We did a temporal resolution refinement study and found that $dt = 1e-04$ was the largest the time step that did not cause a visible difference in the simulation results. It is used in the present paper if it is not specified. Here we give a brief description of the scheme. Rewrite the discretized Burgers' equation as

$$\frac{\partial U}{\partial t} = Res(U), \qquad U(t_0) = U^0, \tag{32}$$

where $Res(U)$ is the residual. Given solution U^n, we obtain solution U^{n+1} using

$$U^{(1)} = U^n + \Delta t Res(U^n), \tag{33}$$

$$U^{(2)} = \frac{3}{4}U^n + \frac{1}{4}U^{(1)} + \frac{1}{4}\Delta t Res\left(U^{(1)}\right), \tag{34}$$

$$U^{n+1} = \frac{1}{3}U^n + \frac{2}{3}U^{(2)} + \frac{2}{3}\Delta t Res\left(U^{(2)}\right). \tag{35}$$

3.3. Initial and boundary conditions

The initial energy spectrum is given in the Fourier space k mimicking the turbulence spectrum Fig. 3. In the present work, the following initial spectrum is used

$$E_0(k) = \begin{cases} A5^{-\frac{5}{3}} & 1 \le k \le 5 \\ Ak^{-\frac{5}{3}} & k > 5 \end{cases}, \tag{36}$$

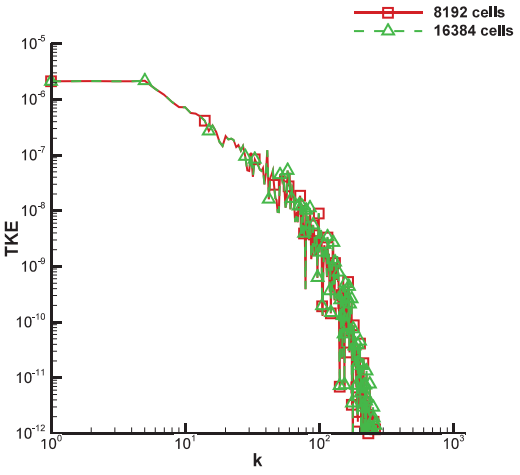

Fig. 4. Turbulent energy spectrum at t=0 and t=T.

where k is an integer varying from 1 to 1280. For each k, the velocity u has a uniformly random phase angle, β, in $[-\pi, \pi]$.

$$u(x) = \sum_{i=1}^{n} (2E_0(k_i))^{\frac{1}{2}} \sin(k_i \pi x + \beta_i) + 1 \tag{37}$$

A is a constant to make the turbulence intensity $\frac{u'}{\bar{u}} = 0.7\%$, where $u' = \sqrt{\frac{\sum_{i=1}^{N}(u_i - \bar{u})^2}{N}}$, $\bar{u} = 1$.

The two boundaries are set to be periodic due to the periodicity of the initial condition.

3.4. Grid and spatial filter

The computational domain is $[-1, 1]$. A mesh refinement study indicated that 8192 cells with the 3rd order FR/CPR method are required to resolve all the scales. Fig. 4 shows the energy spectrum at $t = T$ for two different levels of resolution, 8192 cells and 16,384 cells with the same initial condition and scheme. There is no visible difference between the spectrums. We consider the simulation with 8192 cells with the 3rd order FR/CPR scheme a DNS, and denote $\Delta x_{DNS} = \frac{2}{8192}$.

In the a priori study, the DNS solution is filtered with a box filter with $\Delta = 32\Delta x_{DNS}$. The filtered solution is obtained

$$\hat{u}_{i,\ j} = \sum_{n=1}^{N}\sum_{m=1}^{K+1} u_{n,m} * w_{n,\ m,\ i,\ j}, \tag{38}$$

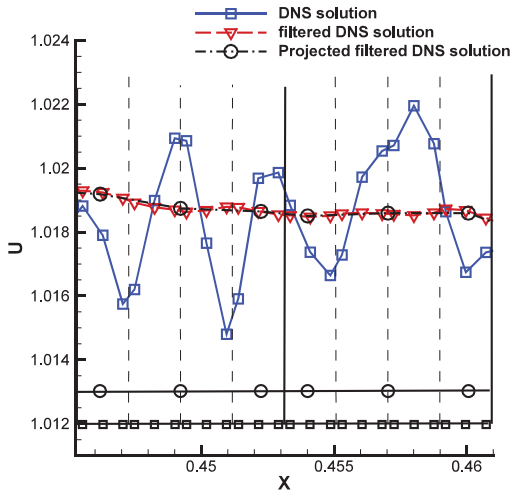

Fig. 5. A comparison of various solutions (square: fine mesh solution points; circle: coarse mesh solution points).

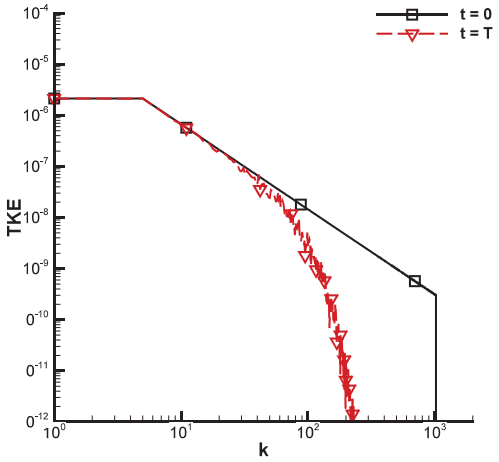

Fig. 6. The energy spectrum at two different times.

Table 1
Correlation coefficients of a priori test.

$\frac{\Delta x_{LES}}{\Delta x_{DNS}}$	SS	DS	SSM	Mix	LUM
1	−0.10	0.6	0.95	0.89	−0.09
2	−0.10	0.6	0.95	0.89	−0.09
4	−0.10	0.6	0.95	0.89	−0.09
8	−0.10	0.6	0.95	0.89	−0.09
16	−0.10	0.6	0.95	0.89	−0.09
32	−0.09	0.59	0.95	0.88	0.04

where N is the number of cells in the filtering stencil of the current degree of freedom and K is the degree of the polynomial of the solution. In each cell, a Gauss quadrature rule was implemented and w is the weighting coefficient. Then the filtered solution on the DNS grid is projected to the (coarse) LES grid if necessary to serve as the LES solution. In the current LES cell, the projected solution at each solution point j is calculated using

$$\int_{\Delta x_{LES}} L_k \sum_{j=1}^{K+1} L_j \hat{u}_{i,j} dx = \sum_{n=1}^{N} \int_{\Delta x_{DNS}} L_k \sum_{j=1}^{K+1} l_j \hat{u}_{n,j} dx, \tag{39}$$

where L_j is the shape function defined based on the solution points of the LES cell, l_j is the shape function based on the solution points of the DNS cell. In the a posteriori study, we do the same thing to the DNS initial condition to generate the LES initial condition.

In Fig. 5, $\Delta = 8\Delta x_{DNS}$, $\Delta x_{LES} = 4\Delta x_{DNS}$ are used to demonstrate the filtering operation. Different cell sizes for LES were tested to evaluate the influence of the truncation error and the SGS modeling error. We call the filter used on the initial condition the first filter and the filter used in deciding the coefficient of the dynamic model or computing the resolved SGS stress the test filter. The test filter width is 2 times the width of the first filter, which makes $\gamma = 2$.

4. Numerical results and discussions

In this section, the results for the a priori and a posteriori tests are presented. Due to the nonlinear convection term, shock waves start to appear after a certain time. Thus all results are obtained at a non-dimensional time $T = 0.05$, when the solution is still smooth. Fig. 6 shows the energy spectrum at t=0 and t=T of the DNS solution. We can see that the high frequencies are damped out by the physical viscosity while the lower frequencies remain.

4.1. A priori tests

Fig. 7 shows the SGS stress computed using different models based on the filtered-DNS data at $t = T$ with various mesh resolutions and a fixed filter width of $\Delta = 32\Delta x_{DNS}$. The ratio between the cell size of LES and DNS is (a) 1, (b) 2, (c) 4, (d) 8, (e) 16, (f) 32. For the SS model, c_s is set to the default value of 0.2 for all of the comparisons. For ILES, the SGS stress is 0 everywhere.

From Fig. 7, we can make some general observations regardless of mesh resolutions:

- No models are able to predict the true stress in both amplitude and phase (peaks and valleys).
- Both the SSM and MM always correctly predict the phase of the true stress.
- SS correctly predicts the phase of the true stress about half the time, and DS agrees with the SS when the phase is correct. When the stress computed with SS has a wrong sign, DS sets the stress to 0.
- LUM agrees very well with SS in SGS prediction with enough grid resolution, but diverges for the coarsest mesh.

Obviously the good phase prediction capability of the MM is due to the dominant SSM term. Next we examine the correlation of the modeled stress with the true stress. Table 1 presents the correlation coefficients between the true SGS and the ones computed with the models. Clearly the SSM and the MM models perform the best. The mesh resolution Δx_{LES} does not have any significant influence on the model behavior, except for LUM. To further evaluate the behavior of these models in an actual computation, we perform a posteriori tests next.

4.2. A posteriori tests

In this test, the filtered 1D Burgers' equation is solved with different models on different meshes with a fixed filter size $\Delta = 32\Delta x_{DNS}$. The results at the same physical time t=T are compared. Fig. 8 shows the SGS stress computed using different models with various mesh resolutions.

In Fig. 8, we can see that the results are very similar to those in the a priori test. We can draw the same conclusions here. Table 2 shows the correlation coefficients for all the a posteriori tests. The SGS stresses computed with SSM and the MM always show high correlations with the true SGS stress. The DS comes second. The SS and the LUM models yield very low correlation with the true SGS stress. LUM diverged for some cases and the correlation is not available. The LES mesh resolution does not have a significant influence on the model behavior, except for LUM.

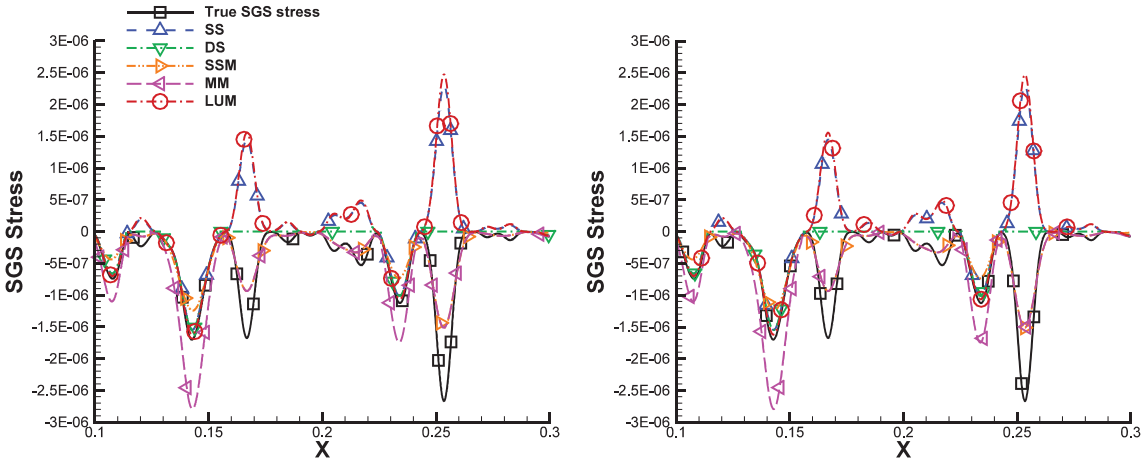

(a) $\frac{\Delta x_{LES}}{\Delta x_{DNS}} = 1$ (b) $\frac{\Delta x_{LES}}{\Delta x_{DNS}} = 2$

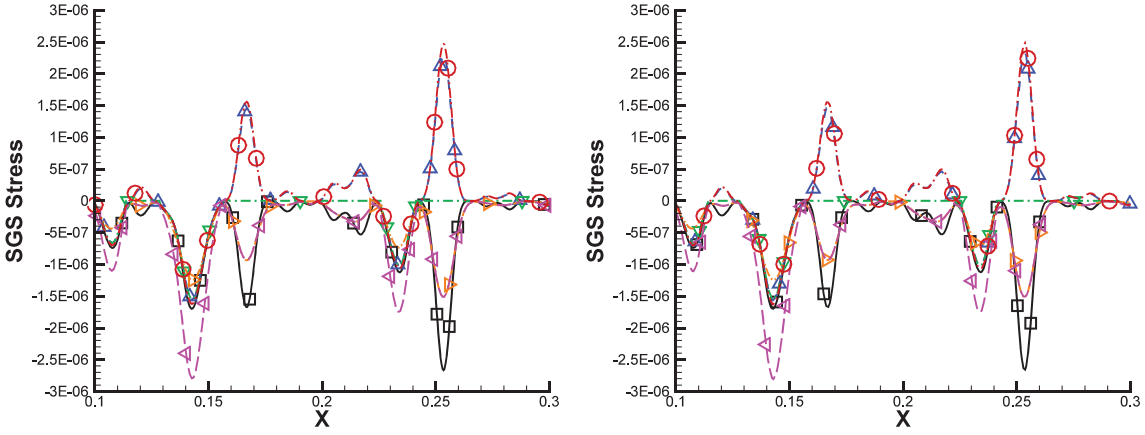

(c) $\frac{\Delta x_{LES}}{\Delta x_{DNS}} = 4$ (d) $\frac{\Delta x_{LES}}{\Delta x_{DNS}} = 8$

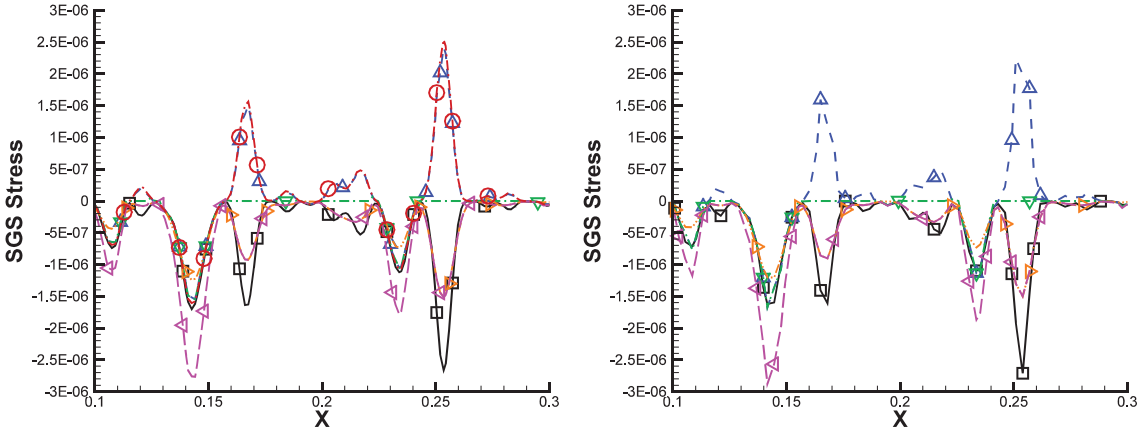

(e) $\frac{\Delta x_{LES}}{\Delta x_{DNS}} = 16$ (f) $\frac{\Delta x_{LES}}{\Delta x_{DNS}} = 32$

Fig. 7. The SGS stress comparison in the a priori tests.

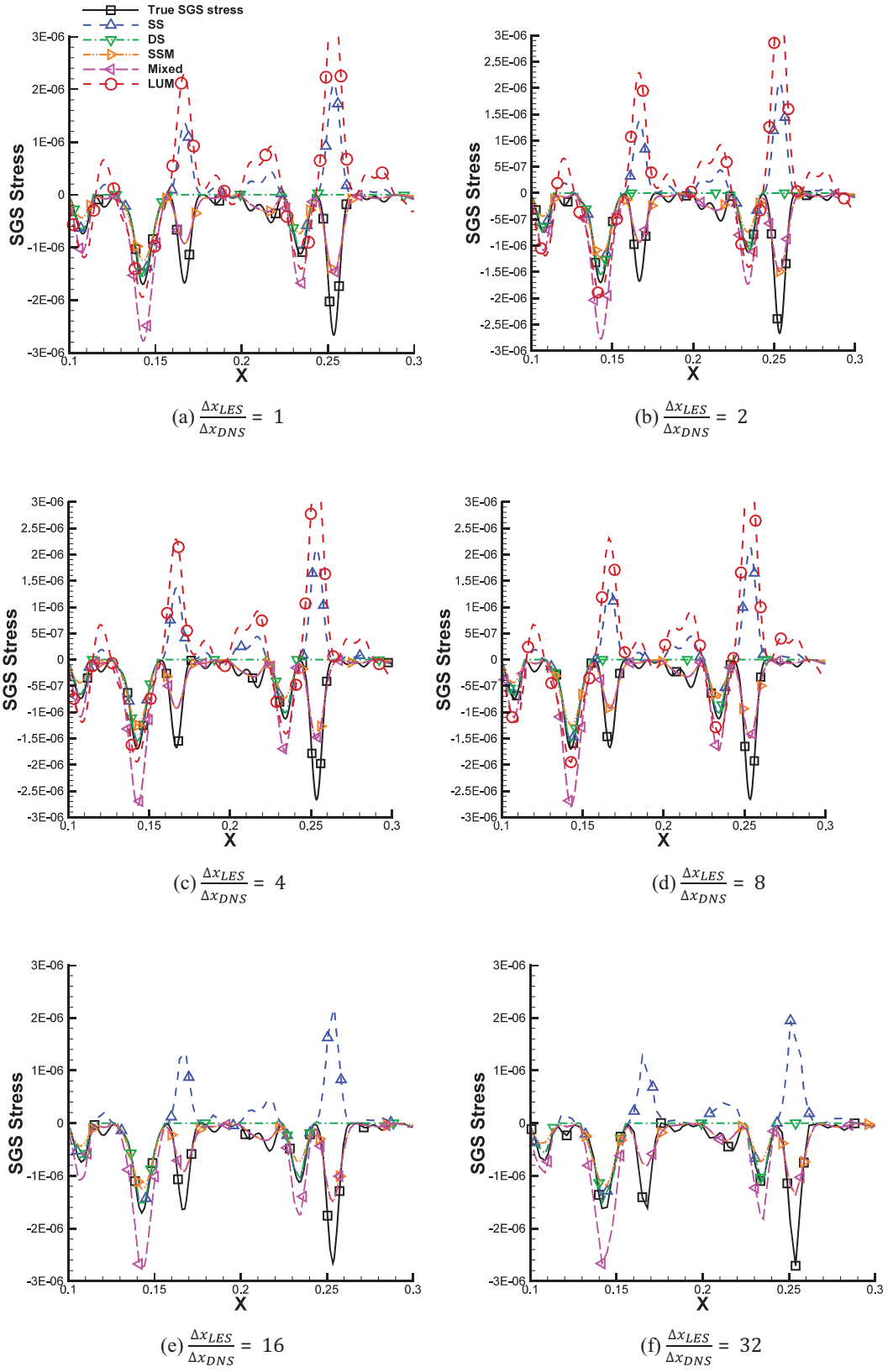

(a) $\frac{\Delta x_{LES}}{\Delta x_{DNS}} = 1$ (b) $\frac{\Delta x_{LES}}{\Delta x_{DNS}} = 2$

(c) $\frac{\Delta x_{LES}}{\Delta x_{DNS}} = 4$ (d) $\frac{\Delta x_{LES}}{\Delta x_{DNS}} = 8$

(e) $\frac{\Delta x_{LES}}{\Delta x_{DNS}} = 16$ (f) $\frac{\Delta x_{LES}}{\Delta x_{DNS}} = 32$

Fig. 8. The SGS stress comparison in the a posteriori tests.

Table 2
Correlation coefficients of a posteriori test.

$\frac{\Delta x_{LES}}{\Delta x_{DNS}}$	SS	DS	SSM	Mix	LUM
1	−0.08	0.6	0.95	0.89	−0.06
2	−0.08	0.6	0.95	0.89	−0.07
4	−0.08	0.6	0.95	0.89	−0.07
8	−0.08	0.6	0.95	0.89	−0.07
16	−0.08	0.6	0.95	0.88	–
32	−0.10	0.57	0.92	0.85	–

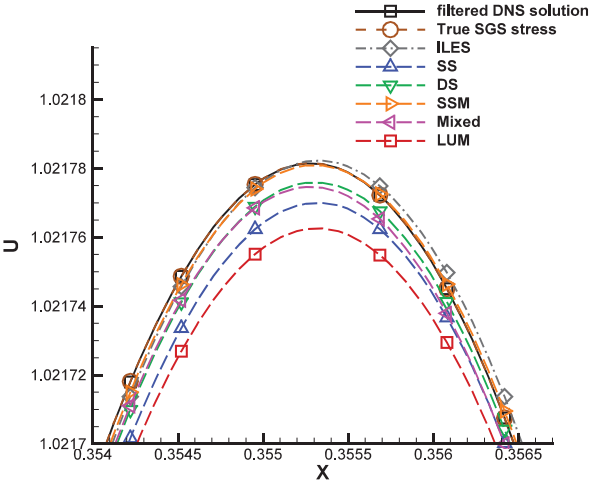

Fig. 9. Solution comparison.

Fig. 9 shows the comparison of the solution, $\hat{u}$, for $\frac{\Delta x_{LES}}{\Delta x_{DNS}} = 1$. The solution computed with the true SGS stress is right on top of the filtered DNS solution. The solutions computed with models and ILES all show differences with the filtered DNS solution. Table 3 shows the L2 norm error comparison. When the LES mesh is sufficiently fine, it is clear that the SSM and the MM produced the best solutions. This is because both models show the best correlation with the true SGS stress. When the LES mesh is coarse, the truncation error is dominant. The results with any model and with the true SGS stress are comparable. Clearly ILES is the best choice because it costs the least.

4.3. Sensitivity of the models to the mesh resolution

Given the fixed filter width, we compare models' behavior on different mesh resolution. Fig. 10 shows different modeled SGS comparison with respect to different Δx_{LES}, (a)SS, (b)SSM, (c)LUM. The ratio$= \frac{\Delta x_{LES}}{\Delta x_{DNS}}$. We can see that in both the a priori and the a posteriori tests, all the models show no sensitivity to Δx_{LES} except for the LUM.

4.4. Investigation of stability of SSM

In Bardina's original paper [10], the SSM was found unstable in some simulations when used with a central finite difference scheme. To remedy the instability, a MM with the DS model was developed to stabilize the simulations. In this section, we show that the extra dissipation added by the MM is not necessary for the FR/CPR method which has embedded numerical dissipation to automatically damp high frequency modes.

We first demonstrate that there is indeed a pile-up of high frequency modes with a central difference scheme in solving nonlinear equations such as the Burgers' equation, while there is no such pile-up with a dissipative high-order FR/CPR scheme. For this purpose, we conduct a numerical study with the initial condition of a single Fourier mode,

$$u(x) = 2(E_0(1))^{1/2}\sin(\pi x) + 1, \tag{40}$$

where $2(E_0(1))^{1/2} = 0.012$. The 1D inviscid Burgers' equation is employed to mimic very high Reynolds number problems. We run the simulation until $t = 26$ when it is right before a shock wave develops. First, the upwind flux and the central flux are employed in the 3rd order FR/CPR scheme to compare their performance. Fig. 11 shows the energy spectrum at $t = 26$ with different mesh resolutions. On the finest mesh, both the central and upwind schemes produced a converged solution within the visible energy spectrum in the figure. On the two coarser meshes, we can see clearly that energy is piling up at high frequencies on those meshes for the simulation with the central flux. But the upwind flux is able to smoothly damp out the high frequency modes so that they are never accumulated to cause stability problems.

Next we test the influence of the SGS models on the energy spectrum. Fig. 12 shows the spectrum comparison of the simulations with and without the SSM and MM. The filter width equals to the cell size. We can see that with the central flux, the SSM neither damps out all the energy accumulated at high frequencies nor accumulates more energy there. Thus the extra dissipation, i.e. the DS, is necessary to stabilize the simulation. It is worth noting that the extra dissipation, in the MM, also damps out the energy at some lower frequencies, which does harm to the resolved large scales.

We also verify that a central difference finite difference scheme behaves similarly with the CPR scheme with a central flux. Fig. 13 indeed shows that the 4th order central finite difference method has a similar performance to the 3rd order FR/CPR scheme with the central flux. This means that for schemes that are not dissipative, more dissipation may be necessary to stabilize the simulations with the SSM model. But for the dissipative ones, such as the FR/CPR method with an upwind flux, no extra dissipation is needed.

4.5. Fourier (von neumann) analysis

To have a better understanding of the final results, we perform an analysis of accuracy and stability of the current numerical scheme. In practice, a finite-difference-like truncation error analysis for the CPR schemes is difficult because each solution point uses a different "scheme". Therefore, we obtain the order of accuracy of a scheme using a Fourier (Von Neumann) analysis. For the sake of simplicity, we consider the following advection equation

$$\frac{\partial u}{\partial t} + \frac{\partial u}{\partial x} = 0. \tag{41}$$

The initial condition is periodic:

$$u_{init}(x) = e^{Iwx} \tag{42}$$

where w is a real number between $--\pi$ and π called the wave number, I is the imaginary unit . The exact solution is

$$u_{exact}(x,\ t) = e^{Iw(x-t)}. \tag{43}$$

The exact time partial derivative is purely imaginary:

$$\left(\frac{du}{dt}\right)_{exact} = -Iw. \tag{44}$$

Denote the solution points in the standard element $[-1,\ 1]$ by $\xi_j,\ j = 1, \ldots,\ K+1$, where K is the order of the solution polynomial. The global solution points are

$$x_{i,\ j} = i + \xi_j/2. \tag{45}$$

Note that

$$u_{i-1,\ j} = e^{-Iw}u_{i,\ j}. \tag{46}$$

Table 3
L2 norm error of the solution.

$\frac{\Delta x_{LES}}{\Delta x_{DNS}}$	True stress	ILES	SS	DS	SSM	Mix	LUM
1	2.03E-08	1.14E-05	1.57E-05	8.88E-06	7.02E-06	6.19E-06	1.80E-05
2	2.13E-08	1.14E-05	1.57E-05	8.88E-06	7.02E-06	6.18E-06	3.02E-05
4	4.60E-08	1.14E-05	1.57E-05	8.88E-06	7.01E-06	6.17E-06	5.62E-05
8	4.91E-07	1.14E-05	1.57E-05	8.97E-06	6.94E-06	6.25E-06	1.07E-04
16	1.09E-05	1.46E-05	2.01E-05	1.49E-05	1.18E-05	1.35E-05	–
32	1.38E-04	1.38E-04	1.41E-04	1.39E-04	1.37E-04	1.39E-04	–

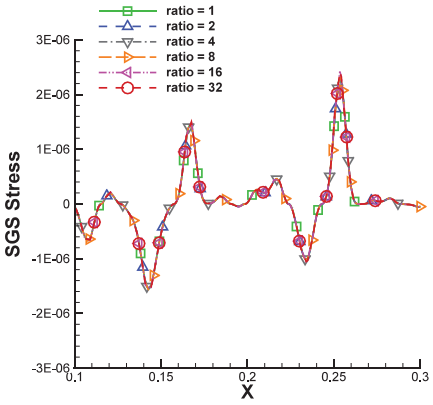

(a) SGS modeled by SS, a priori

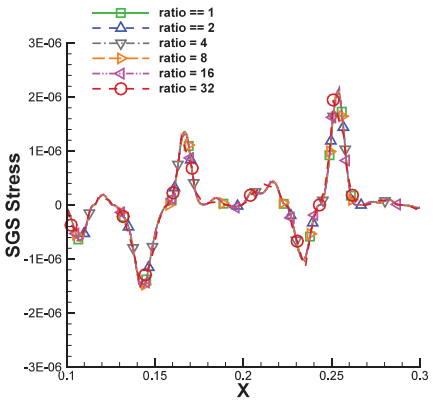

(b) SGS modeled by SS, a posteriori

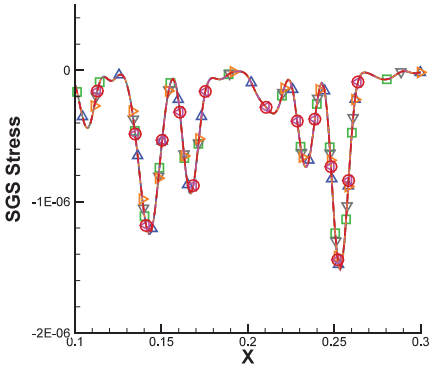

(c) SGS modeled by SSM, a priori

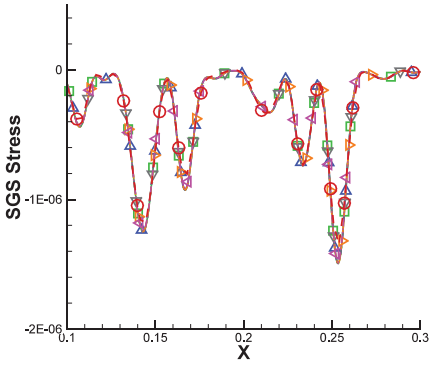

(d) SGS modeled by SSM, a posteriori

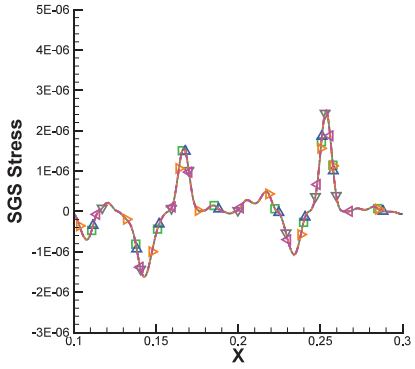

(e) SGS modeled by LUM, a priori

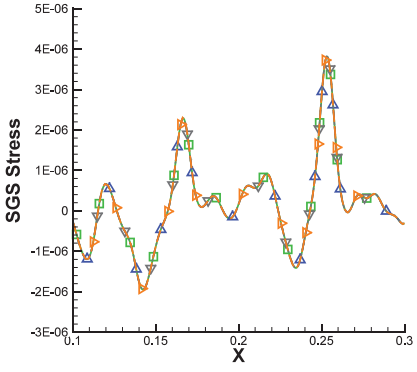

(f) SGS modeled by LUM, a posteriori

Fig. 10. Modeled SGS with different mesh resolution.

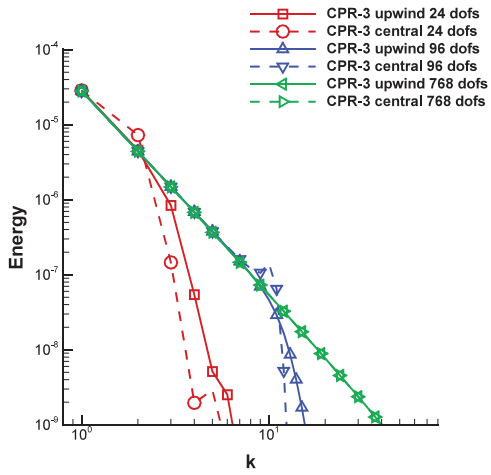

Fig. 11. The spectrum of the upwind flux and the central flux with 3rd order FR/CPR scheme at $\boldsymbol{t} = 26$.

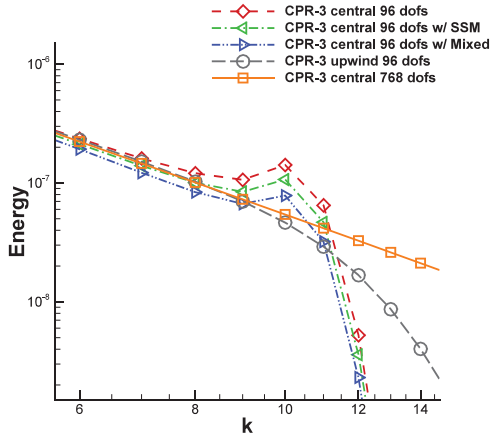

Fig. 12. The spectrum of different models with 3rd order FR/CPR scheme at $\boldsymbol{t} = 26$.

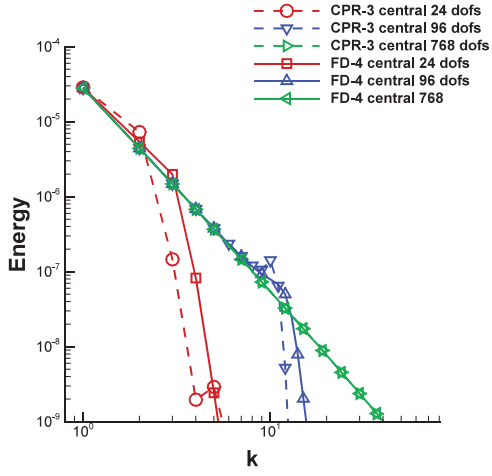

Fig. 13. The spectrum of the 3rd order FR/CPR scheme and the 4th order Finite Difference scheme with the central flux at $\boldsymbol{t} = 26$.

By substituting the solutions to the numerical scheme, we end up with the semidiscretized scheme,

$$\frac{du_i}{dt} = \boldsymbol{S}u_i \tag{47}$$

Table 4
Magnitude of errors.

w	Error
$\frac{\pi}{2}$	1.86E-03
$\frac{\pi}{4}$	3.17E-05
$\frac{\pi}{8}$	5.06E-07

where matrix $\boldsymbol{S}$ is derived from the CPR schemes. $\boldsymbol{S}$ has $K+1$ eigenvalues. The principle eigenvalue approximates $-Iw$,

$$\boldsymbol{S}(w) \approx -Iw. \tag{48}$$

One can expand the principal eigenvalue $\boldsymbol{S}(w)$ as a Taylor series in w.

$$\boldsymbol{S}(w) = -Iw + O\left(w^{K+1}\right). \tag{49}$$

Due to the difficulties in deriving the expression for $\boldsymbol{S}(w)$ when the number of solution points is greater than 2, we obtain the order of accuracy of the current scheme by the following approximation. To estimate the error, we define

$$E(w) = S(w) + Iw. \tag{50}$$

We can estimate the order of accuracy of the scheme by calculating the magnitude of the total error. First, given a series of wave number, each of which is half of the previous one, say $w = \frac{\pi}{2}, \frac{\pi}{4}, \frac{\pi}{8}$. The corresponding magnitude of errors are given in Table 4. Based on the definition, by halving the wave number w, which is equal to doubling the number of mesh points, the error is

$$E(w/2) = S(w/2) + Iw/2. \tag{51}$$

For a scheme to be K-th order accurate, $E(w) \propto O(w^{K+1})$, so we have

$$\frac{E(w)}{E(w/2)} \approx 2^{K+1}. \tag{52}$$

From the table, the order of accuracy of the CPR P2 scheme is 6. Super accuracy is achieved in this analysis. But in general, this property does not hold due to nonlinear errors. The order of accuracy is generally 3 for p=2.

By substituting different values of w, we obtain the two plots below.

The left one shows imaginary part of $E(w)$, which is the dispersion error of the scheme and the right one shows the real part of $E(w)$, which is the dissipation error Fig. 14. We can see with the increase of the wave number, which means the mesh becomes coarser, both of the errors increase. The dissipation error is always negative, which means the scheme is stable for any wave numbers.

4.6. Effects of truncation error vs. SGS model error

In large eddy simulations, the numerical results depend on many factors, including the flow condition, the initial and boundary conditions, the numerical method, the computational mesh, the filter and the SGS model. Some of the factors are physical and others are numerical, and they intertwine to produce the final solution. At the most fundamental level, the filter width Δ in a LES is perhaps the most critical parameter, and Pope discussed the importance of the filter width in [18]. The true LES solution can be obtained by filtering the DNS solution using this Δ. In reality, however, the filter width is often implicitly tied with the mesh size. In such cases, mesh refinement convergence studies become impossible to perform because the filter size is always a variable. One can only see convergence when the mesh size approaches that required of a DNS simulation.

Generally speaking, we want to accurately predict the SGS stress using the numerical solution at the “resolved scale”. The

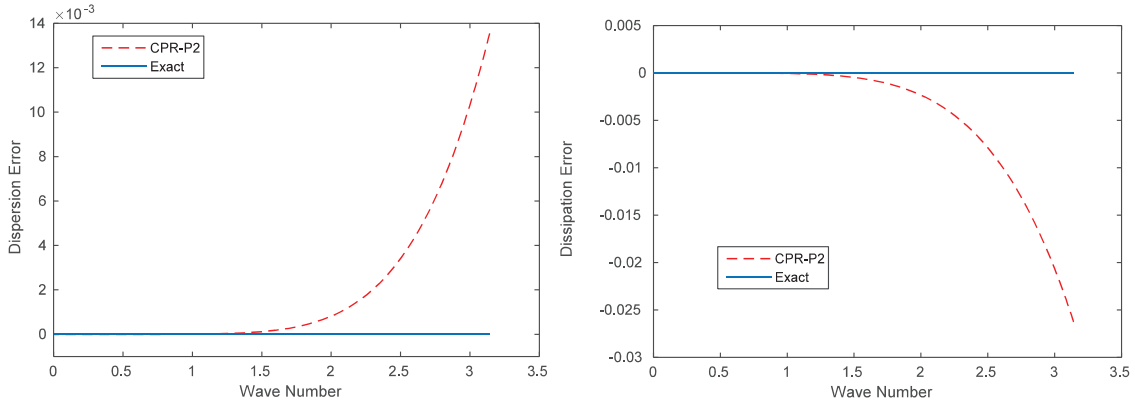

Fig 14. Dispersion and Dissipation error of the CPR-P2 scheme.

filtered solution $\hat{u}$ is always taken to be the solution at the "resolved scale". Let's consider the box filter here. When a solution is filtered with a width Δ, we often state that waves with shorter wavelengths than Δ are filtered out. In fact, waves of wavelengths of 2Δ and 4Δ are heavily damped out too. Based on our analysis, we can see that the amplitudes of 2Δ and 4Δ waves are reduced by 36% and 10% respectively [36]. If we accept 36% filtering error as acceptable, the "resolved scale" should be 2Δ instead of Δ. In addition, numerical methods also have limited resolution depending on the "points per wave" (PPW) or "degrees of freedom per wave" (DOFPW). Let's assume that for the present 3rd order FR/CPR scheme, 9 DOFPW is required to resolve a wave. In other words, 3 elements are needed for a wave since there are 3 DOFs in one element. A truly resolved scale must meet the accuracy requirement from both the filtering operator and the numerical scheme. In this particular case, the resolved scale is

$$S_R = \max(3\Delta x_{LES},\ 2\Delta), \tag{53}$$

In order to have the resolved scale determined by the given filter width, Δx_{LES} should satisfy the following requirement

$$\Delta x_{LES} \leq \frac{2\Delta}{3}, \tag{54}$$

In the case of second-order finite volume methods, each element has 1 solution unknown. If one requires 20 PPW for accuracy, the resolved scale is then

$$S_R = \max(20\Delta x_{LES},\ 2\Delta), \tag{55}$$

If one chooses Δx_{LES} as the filter width, the resolved scale is 20 times larger than the filter width because of the accuracy requirement. In other words, the numerical truncation error is dominant in the LES results. In this case, different SGS models produce nearly the same LES solution as shown in the previous section.

5. Conclusions

In the present study, five SGS models are evaluated with the 1D Burgers' equation discretized with the CPR method. Different LES cell sizes were tested with a fixed filter width. In both the a priori and a posteriori tests on a fine LES mesh, the SSM and the MM showed excellent correlation with the true SGS, while the other models do not predict the SGS stress satisfactorily. However, as the LES cell size increases, numerical truncation error is dominant in the results. In this case, none of the models shows any benefits over ILES.

The stability of the SSM is also investigated on 1D Burgers' equation. The study shows that it is the central flux rather than the SSM that causes energy accumulating at high frequencies, which may lead to the instability of a simulation. In this case, extra dissipation in the form of a DS model, for example, is necessary. However, the schemes with upwind flux smoothly damps out the energy at high frequencies. Thus no extra dissipation is needed to stabilize the simulation with the SSM.

Acknowledgments

The authors gratefully acknowledge the support by NASA under grant NNX12AK04A monitored by Dr. H.T. Huynh and AFOSR under grant FA95501210286 managed by Dr. Fariba Fahroo.

References

[1] Georgialdis NJ, Rizzetta DP, Fureby C. Large-eddy simulation:current capabilities, recommended practices, and furture research. AIAA J 2010;48(8):1772–84.
[2] Durbin PA, Pettersson Reif BA. Statistical theory and modeling for turbulent flows. 2nd ed. A John Wiley and Sons; 2011. Chap 13.
[3] Smagorinsky J, "General circulation experiments with the primitive equations., I. The basic experiment," Weather Rev, 91, pp. 99–164.
[4] Lilly DK, "A propose modification of the Germano subgrid-scale closure method," Phys Fluids A4 pp. 633–635
[5] Germano M, Piomelli U, Moin P, Cabot WH. A dynamic subgrid-scale eddy viscosity model. Phys Fluids A 1991;3:1760–5.
[6] Piomelli U, Liu J. Large-eddy simulation of rotating channel flows using a localized dynamic model. Phys Fluids 1995;7:839–48.
[7] Ghosal S, Rogers MM. A numerical study of self-similarity in a turbulent plane wake using large-eddy simulation. Phys Fluids 1997;9:1729–39.
[8] Akselvoll K, Moin P, "Large-eddy simulation of turbulent confined coannular jets," J Fluid Mech 315:387–411
[9] Wu X, Squires KD, "Large eddy simulation of an equilibrium three dimensional turbulent boundary layer," Am Inst Aeronaut Astronaut. pp. 35:67–74
[10] Bardina J, Ferziger JH, Reynolds WC, "Improved subgrid scale models for large eddy simulation," Am Inst Aeronaut Astronaut pp. 80–1357
[11] Meneveau C, Katz J. Scale-invariance and turbulence models for large-eddy simulation. Annu Rev Fluid Mech 2000;32:1–32.
[12] Huynh HT, "A flux reconstruction approach to high-order schemes including discontinuous Galerkin methods," AIAA paper 2007-4079.
[13] Wang ZJ and Gao H, "A unifying lifting collocation penalty formulation for the euler equations on mixed grids," AIAA-2009-401.
[14] Grinstein FF, Margolin LG. Implicit large eddy simulatio:computing turbulent fluid dynamics. Cambridge, England: Cambridge University Press; 2011.
[15] Moin P, Kim J. Numerical investigation of turbulent channel flow. J Fluid Mech 1982;118:341–77.
[16] Rogallo RS, Moin P. Numerical simulation of turbulent flows. Annu Rev Fluid Mech 1984;16:99–137.
[17] Lesieur M, Métais O, "New trends in large-eddy simulations of turbulence," Annu Rev Fluid Mech pp. 28:45–82
[18] Pope SB, Turbulent flows, Cambridge, England: Cambridge Univ. Press.
[19] Clark RA, Ferziger JH, Reynolds WC, "Evaluation of subgrid–scale models using an accurately simulated turbulent flow," J.Fluid Mech pp. 91:1–16.
[20] McMillan OJ, Ferzinger JH, Rogallo RS, "Tests of new subgrid scale models in strained turbulence," Am Inst Aeronaut Astronaut (AIAA) paper 80–1339.
[21] Ghosal S, Lund TS, Moin P, Akselvoll K, "A dynamic localization model for large eddy simulation of turbulent flows," J Fluid Mech 286:229–255.
[22] Liu S, Meneveau C, Katz J, "Experimental study of similarity subgrid-scale models of turbulence in the far-field of a jet," Appl Sci Res 54:177–190.
[23] Liu S, Meneveau C, Katz J, "On the properties of similarity subgrid-scale models as deduced from measurements in a turbulent jet," J Fluid Mech pp:275:83–119.

[24] Akhavan R, Ansari A, Kang S, Mangiavacchi N, "Subgrid-scale interactions in a numerically simulated planar turbulent jet and implications for modeling," J Fluid Mech 408:pp:83–120.
[25] Wu X, Squires KD, "Numerical investigation of the turbulent boundary layer over a bump," J Fluid Mech pp: 362:229–271.
[26] Haga T, Gao H, Wang ZJ, "A high-order unifying discontinuous formulation for the Navier-Stokes Equation on 3D mixed grid," Math Model Nat Phemon Vol. 6 No. 3, pp. 28–56.
[27] Gao H and Wang ZJ, "A conservative correction procedure via reconstruction formulation with the chain-rule divergence evaluation," J Comput Phys 232, 7–13.
[28] Yu ML, Wang ZJ, "On the connection between the correction and weighting functions in the correction procedure via reconstruction method," J Sci Comput 54, 227–244.
[29] Gao H, Wang ZJ and Huynh HT, "Differential formulation of discontinuous Galerkin and related methods for the Navier-stokes equations," Commun s Comput Phys 13, No.4 1013–1044.
[30] Shi L, Wang ZJ, "A PnPm-CPR method for Navier-Stokes equations," AIAA paper 2012-0460.
[31] Shi L, Wang ZJ, "Adjoint-based error estimation and hp-adaptation for the high-order CPR method," AIAA Paper 2013-0999.
[32] Yu M, Wang ZJ, "On the accuracy and efficiency of several discontinuous high-order formulations," AIAA-2013-855.
[33] Li Y, Wang ZJ, "Evaluation of optimized CPR schemes for computational aeroacoustics benchmark problems," AIAA-2013-2689.
[34] Gopalan H, Heinz S. A unified RANS-LES model:Computational development, accuracy and cost. J Comput Phys 2013;249:249–74.
[35] Bassi F, Rebay S. In: Cockburn Karniadakis, Shu, editors. GMRES discontinuous Galerkin solution of the compressible Navier-stokes equations. Berlin: Springer; 2000. p. 208.
[36] Wang ZJ, Li Y, "An analysis of scale similarity and its implications for large eddy simulation", J Sci Comput (submitted 11.04.16).
[37] Gottlieb S, Shu C-W. Strong stability-preserving high-order time discretization methods. Soc Ind Appl Math 2011;43:89–112.
[38] Li Y, Wang ZJ, "A priori and a posteriori evaluations of subgrid stress models with the burgers' equation", AIAA-2015-1283.
[39] Zang Y, Street RL. A dynamic mixed subgrid-scale model and its application to turbulent recirculating flows. Phys Fluids A 5 1993;3186.
[40] Vreman B, Geurts B. On the formulation of the dynamic mixed subgrid-scale model. Phys Fluids 1994;6:4057–9.